ORIGINAL PAPER

Synthesis and electrochemical performance of nanoporous Li$_4$Ti$_5$O$_{12}$ anode material for lithium-ion batteries

Dan Shao · Jiarong He · Ying Luo · Wei Liu ·
Xiaoyuan Yu · Yueping Fang

Abstract Nanoporous Li$_4$Ti$_5$O$_{12}$ (N-LTO) was prepared by sol–gel method using monodisperse polystyrene spheres as a template and followed by calcination process. The as-prepared N-LTO has a spinel structure, large special surface area, and nanoporous structure with the pore average diameter of about 100 nm and wall thickness of 50 nm. Electrochemical experiments show that N-LTO exhibits a high initial discharge capacity of 189 mAh g^{-1} at 0.1 C rate cycled between 0.5 and 3.0 V and excellent capacity retention of 170 mAh g^{-1} after 100 cycles. EIS and CV analysis show that N-LTO has a higher mobility for Li$^+$ diffusion and a higher exchange current density, indicating an improved electrochemical performance. It is believed that the nanoporous structure has a larger electrode/electrolyte contact area, resulting in better electrochemical properties at high charge/discharge rates.

Keywords Li$_4$Ti$_5$O$_{12}$ · Nanoporous structure · Anode material · Lithium-ion battery

Introduction

Lithium-ion batteries, as a dominant power source for portable electronic devices such as cameras, mobile phones, computers, electric vehicle (EV), and hybrid electric vehicle (HEV), have attracted much attention in the scientific and industrial fields [1–5]. The performance of lithium-ion battery is mainly determined by the properties of the battery active materials (cathode materials, anode materials, and electrolyte materials) [6–9]. The currently commercialized graphite anode cannot satisfactorily meet the safety and rate performance requirements for the future applications, especially in EV and HEV.

Recently, spinel structured Li$_4$Ti$_5$O$_{12}$ (LTO) has attracted much interest due to its potential application as an anode material for high-rate lithium-ion batteries [10–12]. This material has a stable charge/discharge plateau voltage at approximately 1.55 V (vs. Li$^+$/Li), which can avoid the reduction of organic electrolyte and deposition of metallic lithium, thus making batteries more safe. The zero-strain LTO displays small volume change in the charge/discharge process, which makes a structural stability, benefiting for a good reversibility and long cycling life. However, its low electron conductivity greatly influences its discharge ability at high rate. Thus, much efforts have been devoted to modify LTO with metal ion doping (La, V, Na, Mn, Fe, Ni, Cr, and Mg) [13–20], carbon coating [10, 21, 22], or by various controlling particle size to nanometer level [23] and morphologies [24–28] to improve the rate capability. It is of especially interesting to synthesize nanoporous LTO because of several advantages of this geometry listed as follows. Firstly, the open nanopores allow for better accommodation for the volume changes without causing performance deterioration than micron-sized materials (Fig. 1a–c) [29]. Secondly, the nanoporous Li$_4$Ti$_5$O$_{12}$ (N-LTO) can quickly absorb and store large numbers of Li$^+$ ions due to the large surface area and short Li$^+$ diffusion lengths. Furthermore, the N-LTO has short electronic pathways allowing for efficient charge transport.

D. Shao · J. He · Y. Luo · W. Liu · X. Yu (✉) · Y. Fang
Institute of Biomaterial, College of Science,
South China Agricultural University,
Guangzhou 510642, China
e-mail: yuxiaoyuan@scau.edu.cn

X. Yu
Key Laboratory of Renewable Energy and Gas Hydrate,
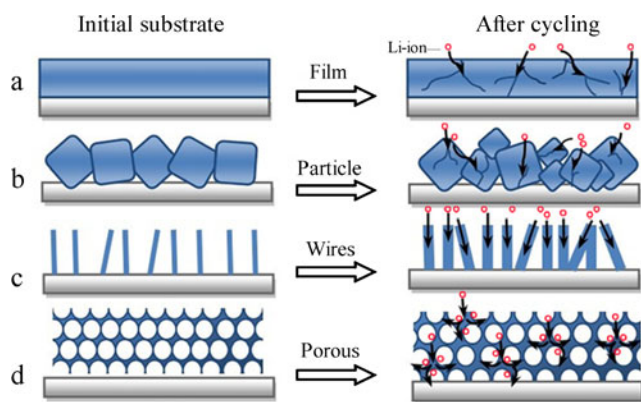Chinese Academy of Sciences,
Guangzhou 510640, China

Fig. 1 a–d Schematic of morphological changes and electron transport that occur in anode material during electrochemical cycling

Herein, we report the synthesis of N-LTO by sol–gel method using polystyrene spheres as templates and followed by calcinating the polystyrene spheres/LTO gel precursor. The physical characterizations and electrochemical properties of this N-LTO for lithium-ion cells have been investigated.

Experiment

Synthesis of N-LTO

Synthesis of monodisperse polystyrene spheres (PS) was described in our previous works [30]. Precursor sol of N-LTO was prepared by dissolving Li acetate (1.4 g A.R.) and tetrabutyl titanate (4.9 g A.R.) in the mixture of 30 ml ethanol (A.R.) and 0.5 ml diethanolamine (A.R.) acted as a chelating agent to slow down the hydrolysis reaction of tetrabutyl titanate [31]. This sol was added dropwise to the surface of the precursor (PS) template, then the sol was infiltrated into the voids between PS particles by vacuum filtration. After that, the deposit was removed from the Buchner funnel, and dried at 60 °C for 4 h. The obtained white solid was the precursor (PS-LTO) of LTO containing PS template. Finally, the precursor was calcinated in air at 400 °C for 4 h with a ramp of 10 °C/min from room temperature to 400 °C, then 750 °C for 10 h. The N-LTO was obtained after cooling to room temperature. For comparison, solid particles of $Li_4Ti_5O_{12}$ (P-LTO) were synthesized by sol–gel method using Li acetate and tetrabutyl titanate as raw materials without the PS template.

Characterization and electrochemical properties

The surface functional groups of the samples were characterized by a Fourier transform infrared spectrometer (FTIR, Nicolet avatar 360 E.S.P.) TA-60 was used for thermogravimetric analysis (TGA) with a heating rate of 15 °C min^{-1} from 50 to 800 °C at air atmosphere. The structures of

products were determined by X-ray diffraction (XRD, D/Max-Ш X-ray diffractometer with Cu Ka radiation). The morphologies of the final products were obtained by scanning electron microscopy (SEM; JEOL JSM-6380LA, Hitachi S-4800). The specific surface area of the prepared sample was evaluated by N_2 gas adsorption and desorption measurements (Gemini-2390, Micromeritics) with Brunauer–Emmett–Teller (BET) method.

Electrochemical performances were tested by assembling CR2025 coin cells in a glove box filled with ultrapure argon, using lithium metal as the counter electrode, 1 mol dm^{-3} LiPF$_6$ dissolved in ethylene carbonate/dimethyl carbonate (1:1, v/v) as electrolyte, and microporous polypropylene film (Celgard 2400) as a separator. The working electrodes were fabricated by mixing as-prepared N-LTO powders (80 wt.%), carbon black (electronic conductive additive, 10 wt.%), and polyvinylidene fluoride (binder, 10 wt.%) in N-methylpyrrolidinone. This slurry was coated on copper foil and dried at 100 °C overnight under vacuum. Galvanostatic charge/discharge tests were performed at room temperature on a LAND CT-2001A cell program-control test system at various rates between cutoff voltages of 0.5 and 3.0 V vs. Li/Li$^+$. Electrochemical impedance spectroscopic (EIS) measurements were carried out on an IM6e electrochemical workstation with an oscillating voltage of 5 mV from 10 mHz to 1 MHz frequency range. The cyclic voltammograms (CV) were obtained using Potentiostat/Gallanostat Model (Perkin-Elmer 273A, EG&E).

Results and discussion

Figure 2 shows the IR spectra of PS, PS-LTO gel, and the N-LTO prepared by carbonizing PS-LTO precursor. In the IR spectrum of PS, the strong characteristic absorption bands appear at 693, 770, 1,600–1,300, 2,923, and 3,037 cm^{-1} are assigned to –(CH$_2$)$_n$– in-of-plane bending vibration, γ(Ar–H) out-of-plane deformation vibration, C=C aromatic skeletal vibration, C–H stretching vibration, and Ar–H stretching vibration of benzenes, respectively. Compared with the IR spectrum of PS-LTO gel composite, as shown in Fig. 2 (c), the characteristic absorption bands of PS disappeared, indicating the complete decomposition of PS template after calcinations at 400 °C for 4 h. The absorption bands at 556 and 1,448 cm^{-1} present the stretching vibration of Ti–O and –CO$_3$, which can be considered as the intermediate during the heating process. Figure 2 (d) shows the IR spectrum of N-LTO and the absorption bands at 678 and 525 cm^{-1} related to the symmetrical stretching vibration and asymmetrical stretching vibration of Ti–O [32, 33], respectively. Meanwhile, the characteristic absorption bands of –CO$_3$ disappeared. The peaks at 3,300 and 1,600 cm^{-1} are due to the absorbed water on the surface of samples [34].
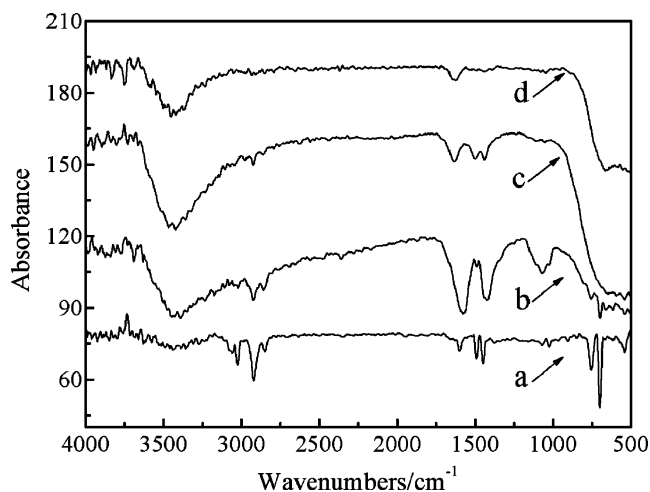
Fig. 2 IR spectra of PS (*a*), the solid precursor PS-LTO gel (*b*), the products obtained by calcination of the precursor at 400 °C for 4 h (*c*), and N-LTO (*d*)

Figure 3 displayed the TGA curves of the mixture consisting of PS and LTO sol from 50 to 800 °C in air atmosphere. The TG curve [Fig. 3 (a)] shows that a small loss of mass occurs in the temperature range from 50 to 200 °C. This effect is due to desorption of water condensed on the sample surface. Also, on the DTG curve [Fig. 3 (b)] at 100 °C an endothermic process starts caused by the melting and followed dehydration of $CH_3COOLi \cdot 2H_2O$ under the influence of crystallization water [35]. Next, on the TG curve between 350 and 420 °C a significant mass loss of the sample is seen, corresponding to the thermal decomposition of PS and a phase transition. This corroborated by a peak on the DTG curve between 350 and 420 °C with a maximum at 410 °C. In the further range from 420 to 470 °C, a mass loss caused by the thermal decomposition of amorphous CH_3COOLi, whereas the curve from 470 to 700 °C mainly corresponds to the crystallization of spinel LTO [10]. As
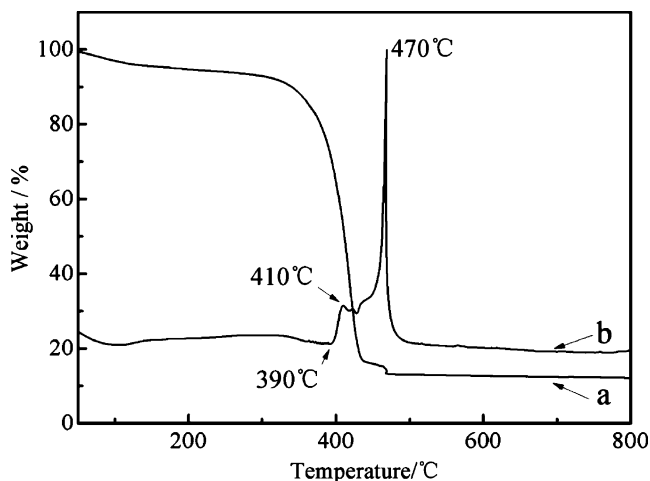
shown in Fig. 3 (a), there was almost no further weight loss at temperature higher than 700 °C.

Figure 4 illustrated the X-ray diffraction pattern of the product obtained by calcination of the precursor at 400 °C for 4 h in air [Fig. 4 (a)] and N-LTO sample [Fig. 4 (b)]. The N-LTO sample has several sharp diffraction peaks at $2\theta=$ 18°, 35°, 37°, 43°, 47°, 57°, 62°, and 66°. These peaks correspond to (111), (311), (222), (400), (331), (333), (440), and (531) planes of a face-centered cubic spinel structure with *Fd3m* space group [36, 37], respectively, which coincides with spinel LTO (JCPDS data card No.49-0207). The unit cell parameter (*a*) calculated by using the software JADE is 0.8382 nm, which is slightly larger than reference value (PDF card *a*=0.8358 nm). As shown in Fig. 4 (a), some diffraction peaks of weak intensity, assigned to TiO_2 phase, were observed. However, no lithium-related phase was detected, suggesting an amorphous structure of the lithium compounds in the product obtained by calcination at 400 °C, according with the TGA results. After the calcination at 750 °C, only the spinel phase was detected, suggesting the successful formation of a phase-pure LTO. Therefore, a high temperature can promote the phase reaction between TiO_2 and the Li-related phase by incorporating Li^+ into the TiO_2 lattice with the formation of LTO [36].

The morphology of PS templates is shown in Fig. 5a. It can be clearly observed that the PS has an average diameter of about 350 nm. SEM image of N-LTO is shown in Fig. 5b. It is obviously found in Fig. 5b that N-LTO is assembled by many nano-hollows. The cavities can be clearly seen from the SEM observation. Fig. 5c displays some representative open hollows, the shells of which are formed by nanoparticles. It could be seen that the pores' average diameter and wall thickness of N-LTO are about 100 and 50 nm, respectively. It implied that the large shrinkage happened in the calcination process. In the images, many cracked shells were
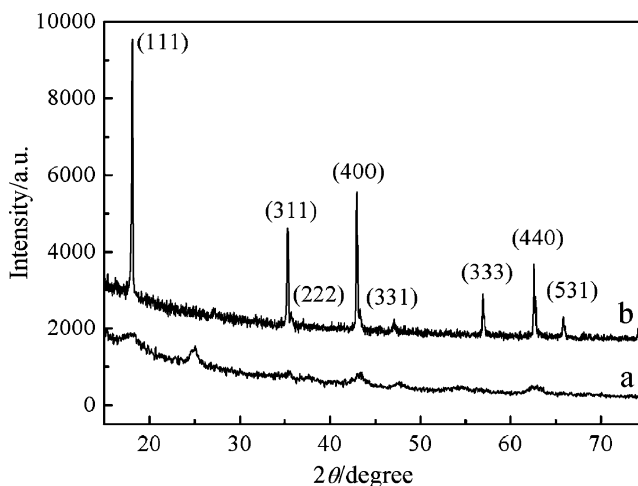

Fig. 3 TG (*a*) and DTG (*b*) curves of the solid precursor PS-LTO gel mixture under air atmosphere

Fig. 4 XRD patterns of N-LTO sample (*b*) the products obtained by calcination of the precursor at 400 °C for 4 h (*a*)
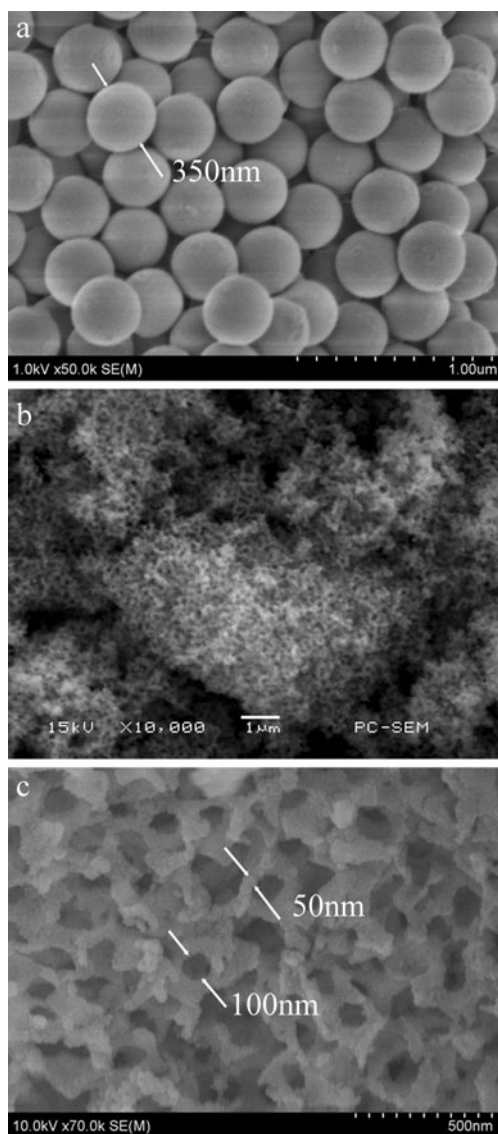
Fig. 5 SEM images of PS (a) and N-LTO (b, c)

found. The cracked shells might be ascribed to the fast escaping of CO_2, H_2O, and CO from the interior of the precursor. The BET surface area of N-LTO particles (19.08 m^2 g^{-1}) significantly exceeds that of the P-LTO powder (1.12 m^2 g^{-1}) and the reported three dimensionally

ordered macroporous $Li_4Ti_5O_{12}$ membrane (8.30 m^2 g^{-1}) [38]. The fabricating process was presented in Fig. 6.

Figure 7 exhibits the initial charge and discharge profiles for the N-LTO sample [Fig. 7 (a)] and P-LTO powder [Fig. 7 (b)] at 0.1 C rate in the voltage of 0.5–3.0 V. The initial discharge capacities of the P-LTO and the N-LTO were 164 and 189 mAh g^{-1}, respectively. The high capacity means that the hollow nanostructure of N-LTO was well developed, and the Li^+-ion insertion and extraction took place at entire part of the porous N-LTO, which originates from the hollow structure and a large specific surface area [28, 39]. However, the N-LTO sample shows a large irreversible capacity at the first cycle. The capacity loss might be attributed to the breakdown processes in the electrolyte solution, such as reduction of trace water, which is more pronounced for high-surface area electrodes [28]. The discharge curve of the N-LTO sample also shows very flat plateau at 1.55 V on a large Li content domain. The very flat plateau indicates the characteristic of two-phase reaction. It has been proposed that Li^+ ions are inserted into $Li_4Ti_5O_{12}$ which converted into $Li_7Ti_5O_{12}$ [40, 41]. The variation of discharge capacity of the N-LTO sample with cycle number at 0.1 C rate is shown in Fig. 8. After the initial cycles, capacity retention is excellent. The discharge capacity of 170 mAh g^{-1} (close to the theoretical capacity of 175 mAh g^{-1} [37]) is obtained after 100 cycles, representing capacity retention of about 100% per cycle during the 10–100th cycle. This excellent capacity performance is mainly due to its nanoporous structure, which allows the electrolyte to penetrate inside N-LTO particles, resulting in high accessibility of the active material [7, 42].

The charge and discharge curves and rate performances of N-LTO electrode at 0.1–10 C are shown in Figs. 9 and 10. It can be seen in Fig. 9 that the cell voltage and discharge capacities both exhibit a tendency to decrease with increasing discharge rates. The N-LTO sample delivers specific capacities of 162, 149, 131, 110, and 102 mAh g^{-1} at 0.5, 1, 2, 5, and 10 C rate, respectively. It can be also noticed in Fig. 10 that as long as the current rate reverses back low current rate, the cell capacity can recover to the original value, indicating that the integrity of the N-LTO anode material has been maintained even after high-rate charge

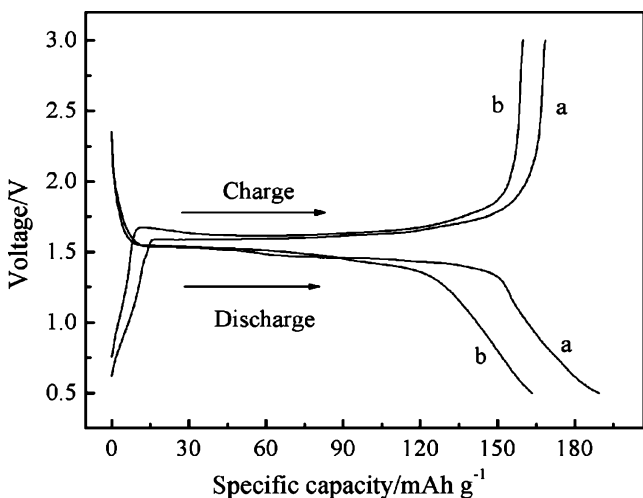Fig. 6 Schematic mechanism for the formation of N-LTO
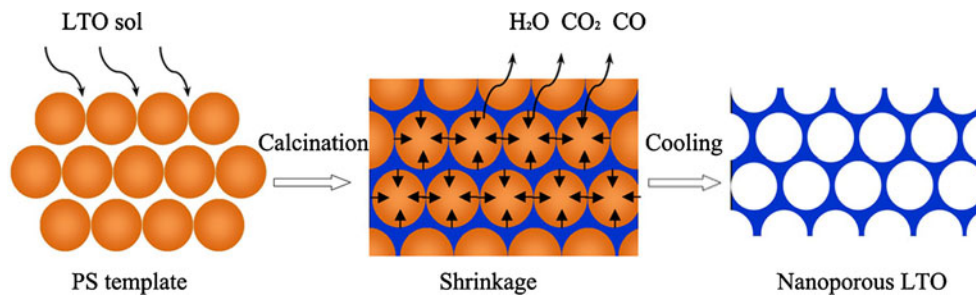
Fig. 7 The initial charge–discharge curves for N-LTO (*a*) and P-LTO (*b*)

Fig. 9 The initial charge and discharge curves of N-LTO at various rates

and discharge. This clearly demonstrates that our hollow nanostructure material architecture is tolerant to varied charge and discharge current, which is a desirable characteristic required for high-power applications. The high-rate capacity performance could be attributed to the nanoparticle distribution. Nanometer-sized electrode material can reduce transport distances for both e$^-$ and Li$^+$ transport makes full Li$^+$ diffusion possible in a short time and at high charge/discharge rates [43].

In order to further investigate the effect of nanoporous structure system on the electrode performance, the EIS of N-LTO (a) and P-LTO powder (b) were measured. As shown in Fig. 11, all the EISs were composed of one semicircle at higher frequencies followed by linear part at lower frequency end. Such EIS patterns can be fitted into an equivalent circuit, as shown in the inset figure. The relationship between the imaginary impedance and the low frequencies is illustrated in Fig. 12. The graph of Z′ against
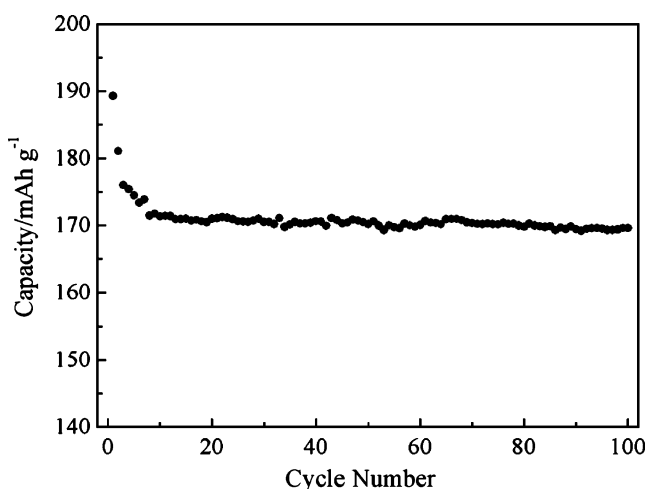
$\omega^{-0.5}$ in the low-frequency region is a straight line with the slope of σ. This relation is governed by Eq. 1 [36]. The diffusion coefficient values (D_{Li}^+) of the Li$^+$ and the exchange current density (i) in the samples are calculated by Eqs. 2 and 3 [44].

$$Z' = R_s + R_{ct} + R_f + \sigma\omega^{-0.5} \tag{1}$$

$$D = 0.5R^2T^2/n^4A^2F^4C^2\sigma^2 \tag{2}$$

$$i = RT/nFR_{ct} \tag{3}$$

where the meanings of σ is the Warburg factor, n is the number of electrons per molecule during oxidization, ω the angular frequency in the low-frequency region, R_{ct} the charge transfer resistance, D the diffusion coefficient, R the gas constant, T the absolute temperature, F Faraday's
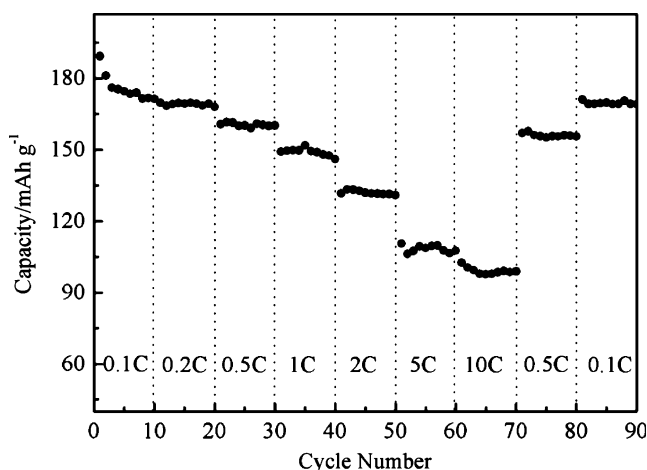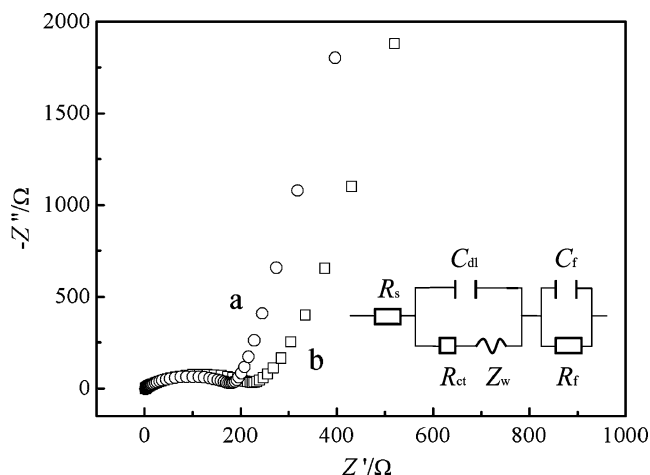

Fig. 8 Cycling performance of N-LTO sample (0.1 C)

Fig. 10 Rate performances of N-LTO

Fig. 11 EISs of N-LTO (*a*) and P-LTO (*b*). The *inset* figure shows the equivalent circuit for the EIS measurement

Table 1 Electrochemical parameters obtained by the electrochemical impedance spectroscopic measurements

Sample	R_{ct} (Ω)	σ (Ω cm^2 S$^{-0.5}$)	D (cm^2 S^{-1})	i (mA cm^{-2})
N-LTO	170	93	2.98×10^{-14}	5.9×10^{-3}
P-LTO	250	126	1.60×10^{-14}	4.0×10^{-3}

insertion and extraction. This indicated that Li$^+$ ions can successfully insert/extract into both materials. Compared with P-LTO electrode, the voltage separation between anodic peak and cathodic peak of N-LTO electrode is smaller, and peak current is larger. These should be due to the higher electrode activity of N-LTO than P-LTO powder, agreeing well with the EISs results.

Conclusions

The N-LTO sample was prepared by using monodisperse polystyrene spheres as templates. The as-prepared N-LTO has a spinel structure, large special surface area of 19.08 m^2 g^{-1}, and nanoporous structure with the pores' average diameter of about 100 nm and wall thickness of 50 nm. Electrochemical performance measurements indicated that the N-LTO electrode material achieved the initial discharge capacity of 189 mAh g^{-1} at 0.1 C rate with excellent capacity retention and rate capabilities. This sample also showed a higher mobility for Li$^+$ diffusion and a higher exchange current density, as indicated by EIS and CV. The result was mainly due to the nanoporous structure and the nanoparticle distribution. Accordingly, the large contact surface area between the anode particle and electrolyte improves the high-rate performance, providing potential as anode material for high-rate lithium-ion batteries.

constant, A the area of the electrode surface, C the molar concentration of Li$^+$, and i the exchange current density.

These calculated results are recorded in Table 1. The obtained D_{Li^+} showed that the N-LTO sample has higher mobility for Li$^+$ diffusion than the P-LTO powder. Furthermore, the exchange current density of the N-LTO sample is higher. From the results of EISs analysis, the nanoporous structure enhanced the conductivity of the samples, which directly led to improved high-rate capabilities of the anode material.

Shown in Fig. 13 are the first cyclic voltammetry curves of N-LTO [Fig. 13 (a)] and P-LTO [Fig. 13 (b)] between 0.5 and 2.5 V with a voltage scan rate of 1 mV/S. Both curves show a pair of reversible redox peaks, which can be observed near the potential of 1.55 V vs. Li$^+$/Li, due to the solid-state redox of Ti$^{3+/4+}$ accompanying with the Li$^+$-ion
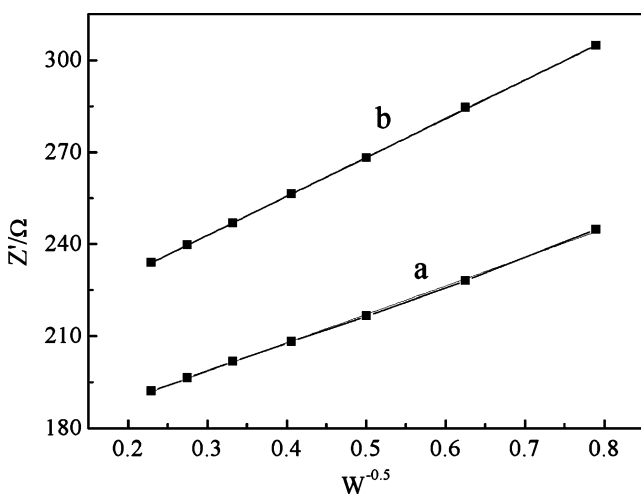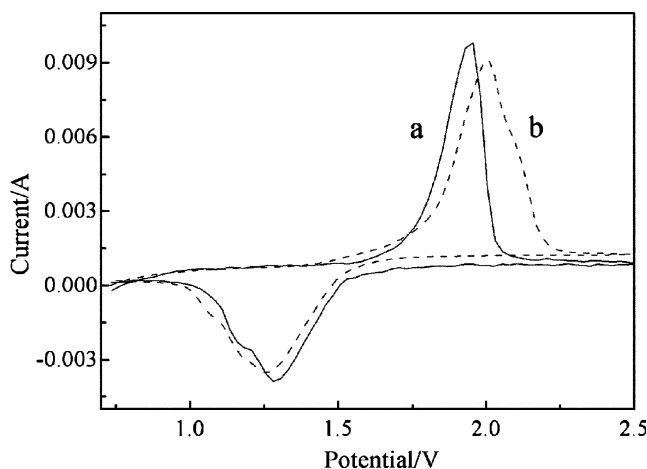

Fig. 12 The relationship between imaginary impedance (Z') and square root of frequency ($\omega^{-0.5}$) in the low-frequency region for N-LTO (*a*) and P-LTO (*b*)

Fig. 13 Cyclic voltagrametric figures of N-LTO (*a*) and P-LTO (*b*)

References

1. Armand M, Tarascon JM (2008) Nature 451:652–657
2. Patil A, Patil V, Shin DW, Choi JW, Paik DS, Yoon SJ (2008) Mater Res Bull 43:1913–1942
3. Kang B, Ceder G (2009) Nature 458:190–193
4. Li H, Wang ZX, Chen LQ, Huang XJ (2009) Adv Mater 21:4593–4607
5. Fergus JW (2010) J Power Sourc 195:939–954
6. Bruce PG, Scrosati B, Tarascon JM (2008) Angew Chem Int Ed 47:2930–2946
7. Guo YG, Hu JS, Wan L (2008) J Adv Mater 20:2878–2887
8. Scrosati B (2007) Nat Nanotechnol 2:598–599
9. Smart MC, Ratnakumar BV, Surampudi S, Wang Y, Zhang X, Greenbaum SG, Hightower A, Ahn CC, Fultz B (1999) J Electrochem Soc 146:3963–3969
10. Lin ZJ, Hu XB, Huai YJ, Liu L, Deng ZG, Suo JS (2010) Solid State Ionics 181:412–415
11. Ju SH, Kang YC (2009) J Power Sourc 189:185–190
12. Wang ZG, Peng WJ, Wang ZX, Li XH, Guo HJ, Wu L (2010) Trans Nonferrous Met Soc China 20:S271–S274
13. Shenouda AY, Murali KR (2008) J Power Sourc 176:332–339
14. Kubiak P, Garcia A, Womes M, Aldon L, Fourcade JO, Lippens PE, Jumas JC (2003) J Power Sourc 119:626–630
15. Chen CH, Vaughey JT, Jansen AN, Dees DW, Kanhaian AJ, Goacher T, Thackeray MM (2001) J Electrochem Soc 48:A102–A104
16. Capsoni D, Bini M, Massarotti V, Mustarelli P, Ferrari S, Chiodelli G, Mozzati MC, Galinetto P (2009) J Phys Chem C 113:19664–19671
17. Ganesan M (2008) Ionics 14:395–401
18. Yin SY, Song L, Wang XY, Huang YH, Zhang KL, Zhang YX (2009) Electrochem Commun 11:1251–1254
19. Hara M, Nakano H, Dokko K, Okuda S, Kaeriyama A, Kanamura K (2009) J Power Sourc 189:485–489
20. Yi TF, Shu J, Zhu YR, Zhu XD, Zhu RS, Zhou AN (2010) J Power Sourc 195:285–288
21. Yuan T, Yu X, Cai R, Zhou YK, Shao ZP (2010) J Power Sourc 195:4997–5004
22. Li X, Qu MZ, Huai YJ, Yu ZL (2010) Electrochim Acta 55:2978–2982
23. Shen CM, Zhang XG, Zhou YK, Li HL (2003) Mater Chem Phys 78:437–441
24. Lin CY, Duh JG (2011) J Alloys Compd 509:3682–3685
25. Lee DK, Shim HW, An JS, Cho CM, Cho IS, Hong KS, Kim DW (2010) Nanoscale Res Lett 5:1585–1589
26. He ND, Wang BS, Huang JJ (2010) J Solid State Electrochem 14:1241–1246
27. Tang YF, Yang L, Qiu Z, Huang JS (2008) Electrochem Commun 10:1513–1516
28. Chen JZ, Yang L, Fang SH, Tang YF (2010) Electrochim Acta 55:6596–6600
29. Chan CK, Peng HL, Liu G, McIlwrath K, Zhang XF, Huggins RA, Cui Y (2008) Nat Nanotechnol 3:31–35
30. Yu SX, Luo GE, Luo Y, Liu W, Yu XY (2011) Adv Mater Res 160–162:1654–1658
31. Yang MM, Yuan JL, Yue P (2008) J Sol–Gel Part Sci Technol 47:115–118
32. Hao YJ, Lai QY, Xu ZH, Liu XQ, Ji XY (2005) Solid State Ionics 176:1201–1206
33. He ZQ, Xiong LZ, Chen S, Wu XM, Liu WP, Huang KL (2010) Trans Nonferrous Met Soc China 20:S262–S266
34. He ZQ, Xiong LZ, Chen S, Wu XM, Liu WP, Huang KL (2010) Trans Nonferrous Met Soc China 20:S257–S261
35. Umbreit MH, Paukszta D (2009) Physica B 404:3620–3636
36. Yuan T, Cai R, Ran R, Zhou YK, Shao ZP (2010) J Alloy Compd 505:367–373
37. Naoi K, Ishimotoa S, Isobea Y, Aoyagi S (2010) J Power Sourc 195:6250–6254
38. Woo SW, Dokko K, Kanamura K (2007) Electrochim Acta 53:79–82
39. Tang YF, Yang L, Fang SH, Qiu Z (2009) Electrochim Acta 54:6244–6249
40. Shen CM, Zhang XG, Zhou YK, Li HL (2002) Mater Chem Phys 78:437–441
41. Cai R, Yu X, Liu XQ, Shao ZP (2010) J Power Sourc 195:8244–8250
42. Amine K, Belharouak I, Chen ZH, Tran T, Yumoto H, Ota N, Myung YK, Sun ST (2010) Adv Mater 22:3052–3057
43. Jiang CH, Zhou Y, Honma I, Kudo T, Zhou HS (2007) J Power Sourc 166:514–518
44. Ji SZ, Zhang JY, Wang WW, Huang Y, Feng ZR, Zhang ZT, Tang ZL (2010) Mater Chem Phys 123:510–515